

Rollover of apparent wave attenuation in ice covered seas

Jingkai Li¹, Alison L. Kohout², Martin J. Doble³ , Peter Wadhams⁴ , Changlong Guan¹, and Hayley H. Shen^{5,6} 

¹Physical Oceanography Laboratory/CIMST, Ocean University of China and Qingdao National Laboratory for Marine Science and Technology, Qingdao, China

²National Institute of Water and Atmospheric Research, Christchurch, New Zealand

³Polar Scientific Ltd, Appin, UK

⁴Department of Applied Mathematics and Theoretical Physics, University of Cambridge, Cambridge, UK

⁵Department of Civil and Environmental Engineering, Clarkson University, Potsdam, New York, USA

⁶DHI-NTU Centre, Nanyang Environment and Water Research Institute (NEWRI), Nanyang Technological University, Singapore Email: hhshen@clarkson.edu. (Corresponding author)

Keypoints:

1. Reduced attenuation at short waves (rollover) is shown with field data to result from wind input and nonlinear transfer between frequencies.
2. The period from which rollover happens increases with distance between the measuring buoys.
3. The apparent attenuation of short waves drops with increasing distance between buoys and increasing wind field.

Keywords: wave attenuation, rollover, field data, WAVEWATCH III[®] simulation.

Abstract

Wave attenuation from two field experiments in the ice-covered Southern Ocean is examined. Instead of monotonically increasing with shorter waves, the measured apparent attenuation rate peaks at an intermediate wave period. This ‘rollover’ phenomenon has been postulated as the result of wind input and nonlinear energy transfer between wave frequencies. Using WAVEWATCH III[®], we first validate the model results with available buoy data, then use the model data to analyze the apparent wave attenuation. With the choice of source parameterizations used in this study, it is shown that rollover of the apparent attenuation exists when wind input and nonlinear transfer are present, independent of the different wave attenuation models used. The period of rollover increases with increasing distance between buoys. Furthermore, the apparent attenuation for shorter waves drops with increasing separation between buoys or increasing wind input. These phenomena are direct consequences of the wind input and nonlinear energy transfer, which offset the damping caused by the intervening ice.

This article has been accepted for publication and undergone full peer review but has not been through the copyediting, typesetting, pagination and proofreading process which may lead to differences between this version and the Version of Record. Please cite this article as doi: 10.1002/2017JC012978

© 2017 American Geophysical Union

Received: Apr 10, 2017; Revised: Aug 21, 2017; Accepted: Oct 05, 2017

1. Introduction

The rapid reduction of sea ice extent and thickness in the Arctic Ocean, has led to increased interest in wave propagation in ice-covered seas. Knowledge of how an ice cover affects ocean wave propagation is needed to guide navigation, engineering and other activities in the more accessible Arctic Ocean. Reviews of theoretical development of wave propagation through ice covers may be found in *Squire* [2007] and *Zhao et al.* [2015].

One of the key problems concerning wave propagation through ice covers is how much incoming waves are damped. Theories based on viscous, viscoelastic, or wave scattering mechanisms have predicted an exponential attenuation over distance, with shorter waves having higher decay rates. Field observations of attenuation, however, sometimes display a ‘rollover’, where attenuation peaks at some wave period, decreasing again at shorter waves. It was first discovered by *Wadhams* [1975] with laser profiles, *Wadhams* [1978] with submarine sonar wave measurements, and *Wadhams et al.* [1986, 1988] with buoy measurements in the marginal ice zone (MIZ) of the Greenland Sea and the Bering Sea. The same phenomenon was found in the MIZ of the Labrador Sea with SAR-derived wave attenuation against wavenumbers [*Liu et al.*, 1991]. The most recent observation of rollover was reported in *Doble et al.* [2015] with buoy data collected in the advancing pancake ice region of the Weddell Sea.

So far, rollover has only been observed in field measurements. In the few laboratory experiments reported, this phenomenon was absent [*Newyear and Martin*, 1998; *Wang and Shen*, 2010; *Zhao et al.*, 2015]. Furthermore, most theoretical models do not predict the rollover of wave attenuation, except for the eddy viscosity model [*Liu and Mollo-Christensen*, 1988]. In that model, the group velocity reaches a minimum at some frequency - though the temporal rate of wave damping due to eddy viscosity is monotonic in frequency, the spatial attenuation demonstrates rollover.

One plausible explanation of the observed rollover is the nonlinear transfer of energy from large to small periods [*Wadhams et al.*, 1988]. *Wadhams* [1986] offered an earlier explanation which may work in some cases. In his simple one-dimensional model of wave scattering the decay rate is critically dependent on floe diameter. The curve of reflection coefficient against floe diameter has a rollover at high frequencies. So if all the floes in an icefield are of similar size the decay of waves in the icefield as a whole follows the general shape of the decay curve for the dominant diameter, giving a rollover. However, if the floes have a range of diameters, the rollover begins at varying periods, and a weighted sum of the decay due to individual floes loses some or all of the rollover.

Another explanation is local wind-wave generation [*Wadhams et al.*, 1988; *Meylan et al.*, 2014; *Li et al.*, 2015]. Using numerical simulation under constant wind and

regular arrays of circular ice floes, *Perrie and Hu* [1996] demonstrated rollover by applying the wave scattering theory of *Masson and Leblond* [1989]. Their study showed that, even though scattering alone predicted a monotonic increase of attenuation with wave frequency, when combined with wind-wave and nonlinear transfer, rollover could be observed in this idealized case. Similar detailed studies of the rollover phenomenon under field conditions have not been conducted to date.

To conduct such a study, *in-situ* wave data from buoys that can survive the harsh environment over long time periods is required. As a supplement to real buoys, wave models may also be used to provide ‘virtual buoy’ data points – though the accuracy of these wave models needs to be substantiated first.

Operational wave models have begun to implement waves-in-ice theories in order to improve their capabilities in ice covered waters. In the past, WAVEWATCH III[®] (WW3) used to treat ice-covered regions as islands [*Tolman*, 2003]. It is now augmented to provide several options (switches) for wave attenuation in ice. These switches include constant wave attenuation (IC1), an eddy viscosity model (IC2), a viscoelastic model (IC3), empirical frequency-dependent damping (IC4), and two scattering models (IS1, IS2). Explanation of these options and relevant references are provided in *Tolman et al.* [2016]. Using IC3 based on a viscoelastic ice model [*Wang and Shen*, 2010], a hindcast was compared satisfactorily with the *in-situ* measurements in the Antarctic MIZ [*Li et al.*, 2015] and in the Beaufort Sea MIZ [*Rogers et al.*, 2016]. The former compared significant wave heights H_s with *in-situ* data reported in *Kohout et al.* [2014]. The latter compared the whole model spectrum with buoy data. Reasonable comparisons were obtained in both cases. Applying the scattering model of *Kohout and Meylan* [2008], the enhanced Wave Model (WAM) from the European Centre for Medium Range Weather Forecasting (ECMWF) also reproduced the wave characteristics measured by buoys in the Weddell Sea [*Doble and Wadhams*, 2006; *Doble and Bidlot*, 2013]. The recent rapid improvements of operational wave models thus provide a possibility to quantitatively study the wave-ice interaction using numerical simulations.

In this paper, we study two contemporary field experiments to better understand the rollover phenomenon. The field experiments - set out in Section 2 - are those reported in (A) *Kohout et al.* [2014]; and (B) *Doble and Wadhams* [2006]. We then perform hindcasts of the two wave events with WW3 in Section 3. A slightly different parameterization of ice viscosity from that used in *Li et al.* [2015] is tested to improve the comparison between the modeled results and observed data. In Section 4, we discuss mechanisms of rollover and show its dependence on distance and wind strength. We summarize the findings in the conclusion section.

2. Rollover in field measurements

Two field experiments are considered here. Case A took place in the Antarctic MIZ in 2012 [Kohout *et al.*, 2014], examining wave damping between the ice edge and deep inside the ice cover. Case B took place in the advancing Weddell Sea MIZ in 2000 [Doble and Wadhams, 2006], with sensors much closer together. The average distance between sensors in case A (sensor K3 & K7) for the duration of the track was 182 km and for case B was 20 km. Sensor locations and tracks are shown in Figure 1(a) and (b) respectively.

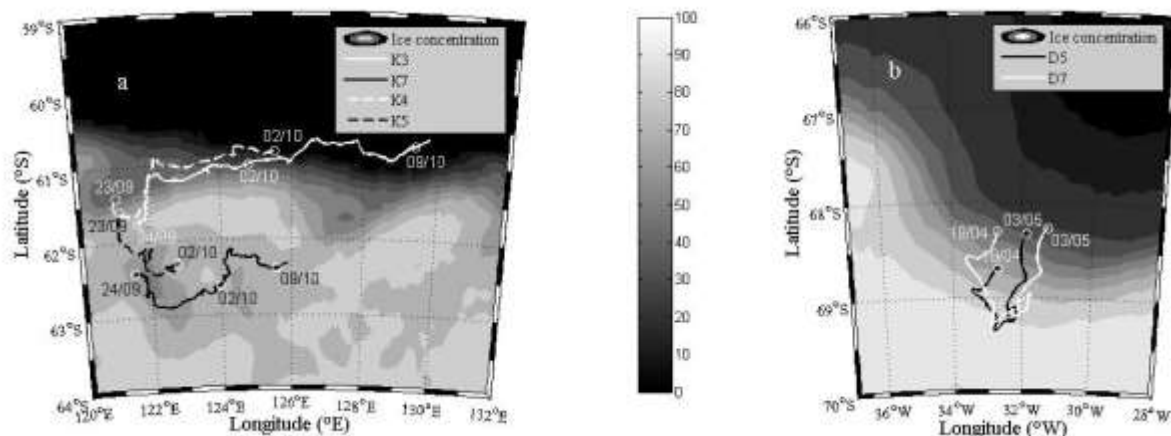


Figure 1. Tracks of (a, case A) four wave sensors with average ice concentration between 23 September and 10 October 2012; (b, case B) two wave sensors with average ice concentration between 20 April and 5 May 2000. White represents 100% concentration, and black represents open water.

Assuming an exponential decay of wave energy with distance through the ice cover, the apparent attenuation coefficient of wave energy is defined as,

$$\alpha(T) = \frac{\ln(PSD_i(T)/PSD_j(T))}{D_{i,j}} \quad (1)$$

where $PSD_i(T)$ and $PSD_j(T)$ are the measured power spectral density (PSD) at two locations. $D_{i,j}$ is the propagation distance of waves between sensors. Following Kohout *et al.* (2014), the distance between sensors $D_{i,j}$ for case A is taken as simply the latitude difference. For case B, $D_{i,j}$ is the distance between buoys along the dominant wave vector. The wave direction was determined from WAM, since the buoys measured only the vertical wave spectra, not its directional distribution.

The apparent attenuation coefficient α with wave period over the duration of the buoy record for the two cases is shown in Figure 2. Both cases exhibit clear rollover. We denote the period corresponding to the maximum α as T_r , the rollover period. It is seen that T_r for case A is greater than for case B. Different ice properties are reported in Kohout *et al.* [2014] and Doble *et al.* [2003]. Case B was characterized by young pancake ice with 0.5~1.5 m in diameter and 0.05~0.3 m thick, while case A was dominantly broken first-year ice floes with 2~20 m in diameter and 0.5~1 m thick. It

is interesting that the younger and thinner pancake ice has one order of magnitude higher α than the much larger first-year floes, as already noted in *Doble et al.*, [2015].

A possible explanation for the lower attenuation in case A is wind-wave generation and nonlinear transfer offsetting the ice damping. This offset is more significant during storms and over a longer distance. As noted earlier, the distance between buoys for case A was nearly an order of magnitude higher than for case B. The differences of various sources between storm and calm cases, defined by a threshold of $H_s = 3$ m, were discussed in *Li et al.* [2015]. Significant wave height H_s for the more seaward buoy in case A exceeded 2 m more than 40% of the time and was greater than 4 m more than 25% of the time [*Kohout et al.* 2014]. In contrast, H_s in case B never exceeded 4 m and only exceeded 2 m for 20% of the total duration. [*Doble and Wadhams*, 2006]. The different rollover periods between the two cases will be discussed later.

It should be noted that the α values shown in Figure 2(a) here and Figure 4 in *Meylan et al.* [2014] are different, even though both studies use the same dataset. In this study a clear rollover of α is seen at $T_r = 8$ s, but in *Meylan et al.* [2014] a monotonically decreasing α was observed. The discrepancy comes from differences in the data used. *Meylan et al.* focussed on the ice damping effect and only considered spectral values greater than 10^{-2} m²/Hz. Conversely, in order to better understand the rollover phenomenon, all measured spectral values are used to generate Figure 2(a) in this study. Low spectral powers are often observed for higher frequency components. They may thus be strongly affected by other mechanisms such as wind input, nonlinear transfer, and dissipation due to turbulence, all may potentially impact rollover. Hence all spectral values are retained in the present study.

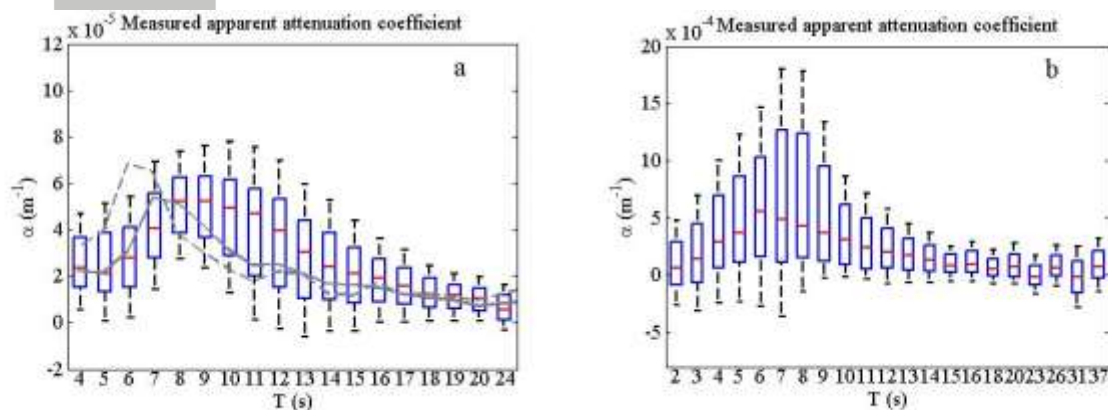


Figure 2. Attenuation coefficient α calculated from measured PSDs. The red line is the median, box height shows the range within which 50% of the data lie, the whiskers give the range of data, outliers are omitted (same in all following boxplots); (a) case A (sensor K3 & K7), (b) case B. Grey solid line in (a) is the measured mean α using data from three pairs of sensors: sensor K4 & K3, sensor K3 & K5, sensor K5 & K7; Grey dash line in (a) is measured mean α using data of two pairs of sensors: sensor K4 & K3, sensor K5 & K7. Comparisons of these different α curves is

discussed in section 4.

3. Hindcast of the wavefield

In order to examine the details of wave attenuation between buoys, a wave hindcast is carried out using WW3 (v5.16). We note that, with the same input and model settings, the simulation result is independent of the model version.

Initialization and parameter settings for the present hindcast are identical to that in *Li et al.* [2015]. Details of the forcing data are given in Table 1. The spatial resolution is much finer than the buoy separation in case A, but too coarse for case B. As will be seen later, this results in a significantly better hindcast for case A than for case B.

Table 1. Forcing data information

	wind	Ice thickness	Ice concentration
Case A	CFSv2 (Saha et al., 2014)	CFSv2 (Saha et al., 2014)	ASI-SSMI (Kaleschke and Kern, 2006)
	3-hr, $0.2^\circ \times 0.2^\circ$	3-hr, $0.2^\circ \times 0.2^\circ$	24-hr, 12.5 km^2
Case B	ECMWF ERA-Interim wind	CFSR (Saha et al., 2010)	ASI-SSMI (Kaleschke and Kern, 2006)
	6-hr, $0.125^\circ \times 0.125^\circ$	6-hr, $0.3^\circ \times 0.3^\circ$	24-hr, 12.5 km^2

For the wave attenuation and dispersion in ice, IC3 is chosen, for which parameterizations of ice elasticity G and viscosity ν are required. In *Li et al.* [2015], $G = 20000 \text{ Pa}$ and $\nu = 0.2 \text{ m}^2/\text{s}$ were used. These constants were chosen because they produced least variance between the measured and simulated H_s out of many different parameter sets tested. Due to the large distance between buoys in case A, significantly different ice conditions may be present. Indeed, the average ice floe diameter increased from 2–3 m at the ice edge to 10–20 m approximately 200 km from the ice edge [*Kohout et al.*, 2014]. Considering such a change of ice conditions, a variable viscosity depending on ice thickness is therefore tested here to determine whether it compares better with measured data. The same idea was examined in *Doble et al.* [2015]. Here we try a quadratic fitting $\nu = 0.88h^2 - 0.015h$ with an average ν for $h \leq 1 \text{ m}$ about $0.2 \text{ m}^2/\text{s}$, the same as the constant used in *Li et al.* [2015]. The elastic parameter G is kept at 20000 Pa . For case B, because of the shorter distance between the buoys, constant $G = 5000 \text{ Pa}$ and $\nu = 0.5 \text{ m}^2/\text{s}$ are applied, based on the fact that in case B the ice was weaker and with higher measured α . We emphasize that the parameter setting here is not the result of a formal optimization procedure, but only by choosing the closest match to measurements from the cases tested.

The simplified governing equation for the wave energy propagation is

$$\frac{\partial N}{\partial t} + \nabla_x \cdot \dot{x}N + \frac{\partial}{\partial k} \dot{k}N + \frac{\partial}{\partial \theta} \dot{\theta}N = \mathbf{S}_{tn} + \mathbf{S}_{in} + \mathbf{S}_{nl} + \mathbf{S}_{ds} + \mathbf{S}_{ice} \quad (2)$$

where $N = N(t, x, y, k, \theta)$ is the wave action density as a function of time t , space x and y , wave number k and direction θ . The linear input term \mathcal{S}_{in} relates to model initialization. \mathcal{S}_{in} , \mathcal{S}_{nl} , \mathcal{S}_{ds} and \mathcal{S}_{ice} represent wind input [Tolman and Chalikov, 1996], nonlinear interaction [Hasselmann *et al.*, 1985], dissipation [Tolman and Chalikov, 1996] and sea ice effects [Wang and Shen, 2010] respectively. During the calculation, \mathcal{S}_{in} and \mathcal{S}_{ds} are scaled by $(1 - C)$ and \mathcal{S}_{ice} is scaled by C , the ice concentration.

Figure 3(a,b) shows the improvement in modeled H_s with the updated viscosity parameterization for case A. Modeled results with a constant viscosity are in black and with quadratic viscosity parameterization are in red. Comparing these two modeled H_s for sensor K3 close to the ice edge (black and red solid lines) we find no obvious change. For short propagation distance from the ice edge, the effect of a variable viscosity is negligible. But for sensor K7 far inside the ice cover (black and red dashed lines), the new modeled H_s values are closer to the measurements. For calm cases with $H_s < 1$ m, mean errors between modeled and measured H_s are reduced by 30% from the constant viscosity results. This result suggests the necessity of relating the viscoelastic parameterization to ice properties. Comparison of measured and modeled H_s for case B is shown in Figure 3(c). In this case, this simulation cannot distinguish the two sensors. With the forcing wind field at a spatial resolution of $0.125^\circ \times 0.125^\circ$, ice thickness field at a spatial resolution of $0.3^\circ \times 0.3^\circ$, and mean buoy distance of 20 km, this result is not surprising. Modeled H_s for both sensors is close to the measurement at sensor D7. By choosing different G and ν , results may approach sensor D5 instead. The measured data for the two sensors are quite different, however. A similar spread of significant wave height from nearby (in space and time) buoys was also observed in a recent study [Rogers *et al.* 2016, Figure 2]. Finer scales of wind and ice variability are strongly reflected in closely-spaced buoy data. To discuss the hindcast further, we will focus on case A with the quadratic formulation for ν .

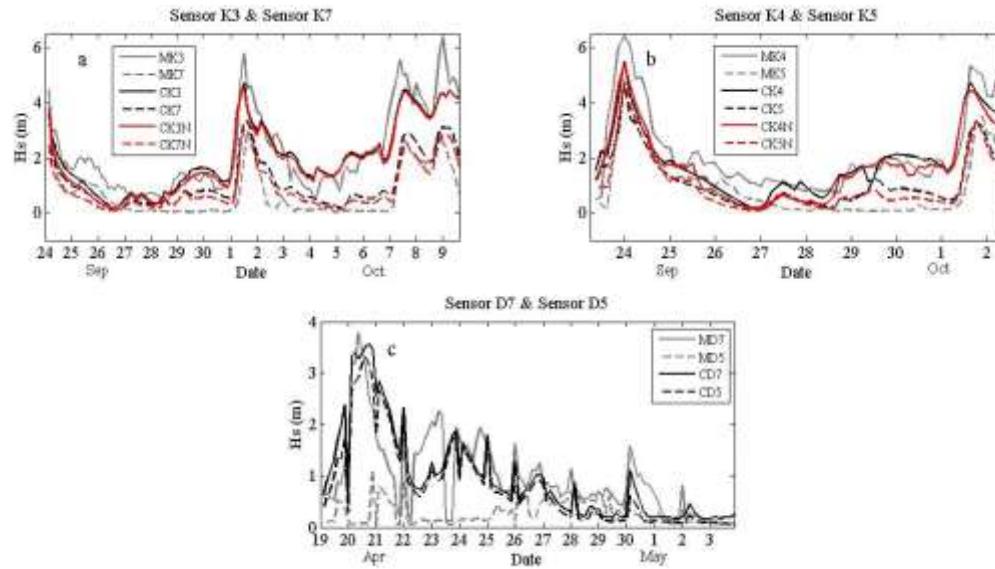


Figure 3. Comparisons of significant wave height H_s from buoy measurement (M) and WW3 model calculation (C): (a) case A, sensor K3 to K7; (b) case A, sensor K4 to K5; (c) case B, sensor D7 to D5 (measured: grey, simulated: black-constant viscosity and red-variable viscosity, near ice edge: solid line, inside ice cover: dash line).

Figure 4 shows comparisons between measured and modeled PSD at sensors K3 and K7. Four examples are selected here: two storm cases (b & f and d & h) and two calm cases (a & e and c & g). Model results generally follow the spectral shape of the buoy measurements well and storm cases fit better than calm cases. For calm cases (e) and (g), the bulk of the modeled PSD overestimates the measured wave energy, implying a stronger damping capability of sea ice than modeled. However, at longer periods, the modeled wave energy density is significantly less than measured, while the opposite is true at shorter periods. For longer periods, as discussed in *Tolman et al.* [2016] parameterization of source terms are sensitive to swell, which dominates in calm conditions. Hence under calm conditions the discrepancy between modeled and measured wave energy for long waves is accentuated. For shorter periods, there are several probable reasons for the lack of agreement between modeled and measured energy. Firstly, short waves are easily affected by uncertainties in local wind and ice properties from the model input. Secondly, in the current model, wind input S_{in} and white-capping dissipation, S_{ds} , are both scaled by $(1 - C)$; hence both the input *via* wind and the dissipation *via* white-capping are absent in the presence of ice. These assumptions have not been rigorously proven based on physical principles or validated from direct measurements. In fact, both overestimating [*Doble and Bidlot*, 2013] and underestimating [*Rogers et al.*, 2016] energy at short waves have been demonstrated in model studies. Despite these discrepancies at the low and high period ends of the spectra, the general agreement of modeled and measured data is encouraging.

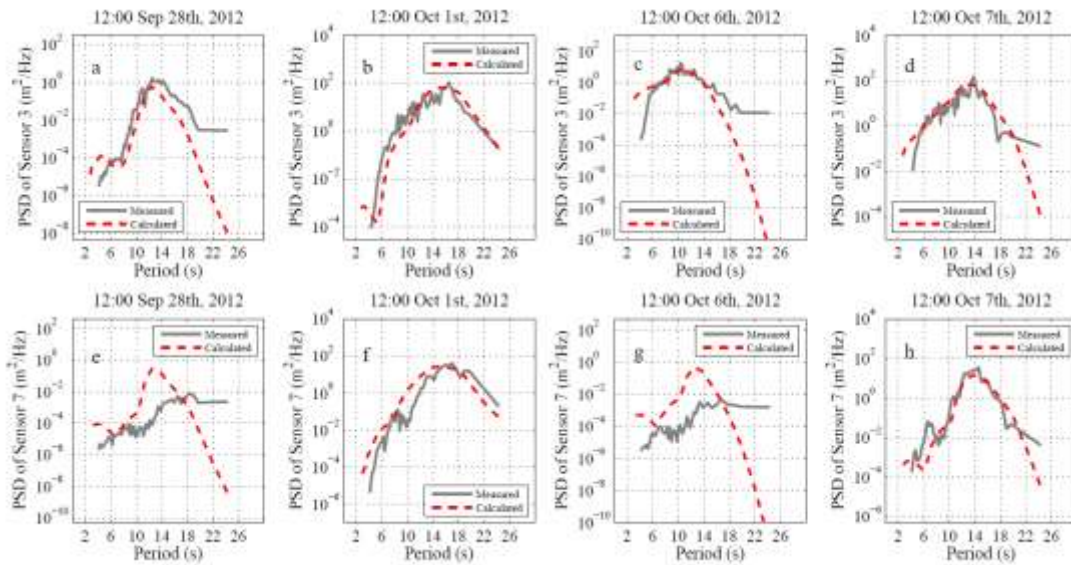


Figure 4. Comparison plots of power spectral density between buoy data and modeled results with the variable viscosity for selected times (a-d are sensor K3, e-h are sensor K7). As in Figure 3, results are shown for the buoy measured (grey line) and calculated using IC3 for S_{ice} (red dash line).

Using the modeled PSD over the entire deployment period, the calculated apparent attenuation coefficient α between sensor K3 and K7 is shown in Figure 5. The measured median attenuation from Figure 2(a) and the theoretical damping due to ice alone are superimposed. Sensors K3 and K7 are chosen because they represent the maximum propagation distance and longest time series. Comparing model results (boxplot) with the measured data (grey dashed curve), significant differences between measured and modeled α appear between 9 and 17 seconds: the measured α is much greater than the modeled value. As shown in Figure 4, 9 to 17 seconds waves hold much of the total wave energy, especially in storm cases. There are two probable reasons for this discrepancy, one concerns the ice edge and the other far inside the ice cover. Near the ice edge, missing extreme wind in the reanalysis data may lead to underestimation of peak energy as apparent in Figure 3 (a-b). Far inside the ice cover, as a result of the overestimated wave energy shown in Figure 3 (a-b) and Figure 4 (e-h), the modeled ice damping is reduced even if the PSD near the ice edge agreed with the measurement. Notwithstanding these issues, the model reproduces the occurrence of rollover quite well. We thus proceed using WW3 results to further investigate the rollover behavior in the next section.

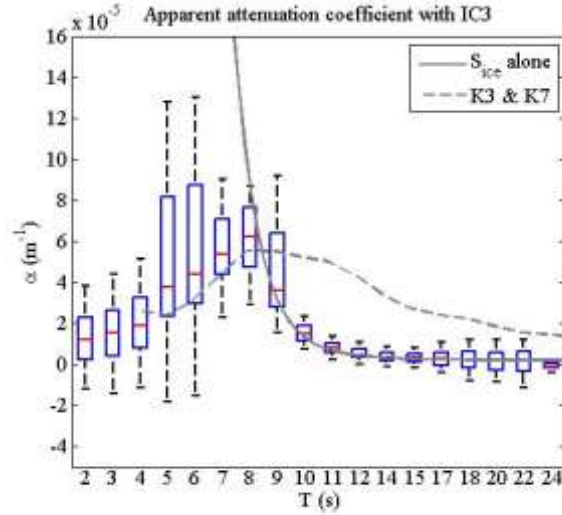


Figure 5. Comparison of α between sensor K3 and sensor K7 from model results (boxplots) using WW3 and the measured data. The grey dash line reproduces the median measured α values of Figure 2(a). The grey solid line is the calculated α due to S_{ice} alone using the viscoelastic model [Wang and Shen, 2010], with an average ice thickness of 0.75 m, ice concentration of 0.65, deep water condition, and $G = 20000$ Pa, $\nu = 0.2$ m²/s.

4. Discussion

Adopting the viscoelastic model, wave attenuation S_{ice} due to ice alone may be obtained by solving the velocity potential $\phi \sim e^{i(k_r + ik_i)x - i\sigma t}$ [Wang and Shen, 2010]. The relation between the energy attenuation coefficient α and the imaginary wave number k_i is [Cheng et al., 2016; Rogers et al., 2016]:

$$\alpha = 2k_i C \quad (3)$$

shown as the grey curve in Figure 5. It represents how S_{ice} damps waves energy without the influence of other source terms. It is clear that S_{ice} alone does not produce rollover. Taking a 6 s wave as an example, the theoretical attenuation due to the ice effect is greater than 10^{-4} m⁻¹. Based on this exponential decay rate, a 6 s wave with an amplitude of 3 m would have a wave height of only 0.14 mm after propagating 100 km through ice (less than the distance between buoys in case A). The measured energy of short waves far inside the ice cover thus comes mainly from the other sources: $S_{in} + S_{nl} - S_{ds}$. Among these three terms, it was found that S_{ds} was much smaller than the other two terms [Li et al., 2015]. Along the path of wave propagation, S_{in} and S_{nl} effectively offset the pure damping due to S_{ice} . This is the mechanism that results in the rollover phenomenon, as suggested in Wadhams et al. [1988] and Bennetts and Squire [2012], as well as proven in an idealized model by Pierre and Hu [1996].

As discussed earlier, over long distances, ice properties may vary significantly. A

variable viscosity such as the quadratic ν and h relationship used in Figure 3 may be needed to better model the wave energy evolution. Numerical tests show that variations of ice parameters (C , h , and ν) only change the α curve (grey solid line) quantitatively, not its monotonically declining shape. Hence, for simplicity, averaged ice parameters were used to obtain α corresponding to \mathcal{S}_{ice} alone in Figure 5. We further tested the sensitivity of rollover observed in the apparent attenuation to details of \mathcal{S}_{ice} by using a constant $\nu = 0.2 \text{ m}^2/\text{s}$. Again the resulting boxplot only changed slightly (not shown here). The insensitivity of behavior of α with respect to details of \mathcal{S}_{ice} indicates that parameterization of \mathcal{S}_{ice} is not the key reason leading to rollover phenomenon, but \mathcal{S}_{in} , and \mathcal{S}_{nl} are the main contributors.

In addition to reducing the apparent wave attenuation, the two source terms \mathcal{S}_{in} and \mathcal{S}_{nl} also produce an interesting pattern of rollover. As Figure 1(a) shows, tracks of four sensors are all roughly parallel to the ice edge. Using the measured PSDs during those days, it is possible to examine how rollover changes with different propagation distance through the ice cover. Grey solid line in Figure 2(a) shows calculated α using three pairs of adjacent sensors from north to south and grey dash line in Figure 2(a) shows α calculated from only two pairs of sensors with short inter-buoy distances. Comparing these two curves with the boxplot in Figures 2(a), of which the α values are from sensor K3 and K7 with largest separation, the average propagation distance, D , through sea ice in case A satisfies $D_{\text{fig.2(a)(boxplot)}} > D_{\text{fig.2(a)(grey solid line)}} > D_{\text{fig.2(a)(grey dash line)}}$. Correspondingly, the rollover period in these three plots changes from $\approx 8 \text{ s}$, $\approx 7 \text{ s}$, to $\approx 6 \text{ s}$, respectively. It clearly shows the positive correlation between the propagation distance through ice covers and the rollover period.

In order to check if this relation is a general phenomenon, a numerical test is done for both case A and B using WW3. Starting from the wavebuoy at the ice edge (sensor K3 for case A and sensor D7 for case B), a number of ‘numerical sensors’ are deployed southward every 0.1 degree. Using the modeled PSD at each of these locations, the calculated α with different $D_{i,j}$ can be obtained. To smooth the attenuation curve, Figures 6(a) and 6(b) show the five-point moving average of the calculated α from two selected times in case A, corresponding to storm and calm case, respectively. Figure 6(c) shows the five-point moving average of one selected time in case B. Black arrows indicate how α curves change as $D_{i,j}$ increases, red dash lines follow the rollover period.

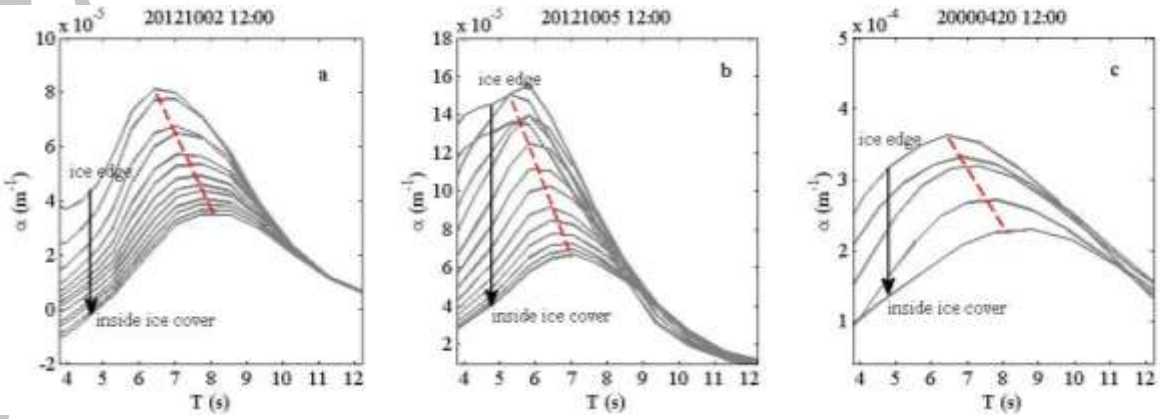


Figure 6. Five-point moving average of attenuation coefficient α with different propagation distances calculated from WW3 for selected times in case A (a, b) and case B (c). Case (a) corresponds to storm events and case (b) corresponds to calms. Each curve is the result of a pair of sensors with increasing distance between them, one fixed near the ice edge and the other southward at an increment of 0.1 degree.

This numerical experiment demonstrates that rollover period increases as $D_{i,j}$ increases for all cases. By comparing Figure 6(a), (b) and (c) and other tests with different G and ν , we also find that this behavior is independent of G and ν parameterization as long as ice damping is strong. For short waves, as $D_{i,j}$ increases, its apparent attenuation coefficient α deviates from the exponential decay theory. Apparent attenuation can even be negative, such as seen at 12:00 on 2nd Oct, 2012 for 4 second waves. In this case, the ice concentration at these locations was low, allowing more effective wind-wave generation inside the ice edge. Wavebuoys far inside the ice cover thus measured even higher energy than those near the ice edge.

As we have seen, the two sensors in case B have a much shorter inter-buoy distance than case A, suggesting that short waves may not be ‘fully damped’ by the ice when they reach the inside sensor. Taking the 6 s wave as an example once again; in case A, according to the previous discussion, it should be fully damped at the inside sensor location if we only consider the ice damping effect. Thus the majority of the measured energy at the inside sensor location comes from the accumulated \mathcal{S}_{in} and \mathcal{S}_{nl} effects. The measured α is therefore smaller than from \mathcal{S}_{ice} alone. While in case B, contributions from these two source terms are less, due to the short distance between buoys, thus the apparent attenuation α is closer to that which would be expected by \mathcal{S}_{ice} alone. This conclusion also implies that the rollover phenomenon will be more prominent in observations over longer wave propagation paths. A by-product of this phenomenon is that the larger the separation distance between the buoys, the smaller the measured apparent attenuation α of short waves as observed in Figure 6.

To further demonstrate the \mathcal{S}_{in} effects, we test the strength of wind field on the apparent attenuation. We scale the CFSv2 wind data by a factor R and keep the rest of the simulation parameters the same as before. Figure 7 shows the resulting α between K3 and K7, averaged over the duration of the field experiment. As expected, when

wind is stronger, the rollover period is larger and the apparent attenuation is lower. The increasing of T_r slows down as wind keeps growing, due to the evolving relative importance of S_{in} as wave periods grow. The behavior shown in Figure 7 remains qualitatively the same even when we limit R to the ice covered region only.

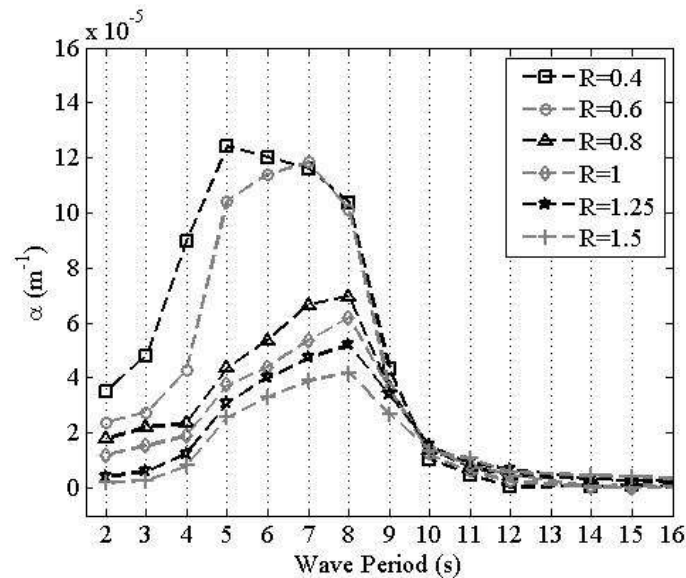


Figure 7. Simulated attenuation coefficient α (between K3 & K7 for case A) by WW3, with different strengths of wind field for case A, where the wind field is from CFSv2 and scaled by the factor $R = 0.4, 0.6, 0.8, 1, 1.25, 1.5$.

5. Conclusion

Inspired by the persistent rollover of wave attenuation from field observations, WW3 is adopted to create virtual buoys to study details of the wave propagation under ice covers. The model results are first validated by comparing with two field experiments in the Antarctic MIZ. Two ice attenuation models based on a viscoelastic theory are compared: one assumes constant viscosity and one assumes thickness dependent viscosity. When buoys are far apart, the latter model improves comparisons between modeled and measured significant wave height. For buoys that are close together, the local variabilities of the wind and ice conditions - not captured in the model simulations - result in differences between modeled and measured wave energy. The model results show clearly that, although the attenuation due to ice monotonically decreases with increasing wave period, the apparent attenuation coefficient peaks at some period. This rollover phenomenon appears to be insensitive to the damping model, including the two tested in this study and the one using the scattering mechanism [Pierre and Hu, 1996]. We find that as long as the input from wind and nonlinear transfer overcomes the ice damping, a rollover will occur. Furthermore, the availability of buoy data for long durations and over large areas showed a positive correlation between wave propagation distances and rollover periods. That is, the period corresponding to peak attenuation increases with buoy separation. Virtual buoys generated with a WW3 simulation show this behaviour clearly. Furthermore, it

is also shown that the apparent attenuation of short waves decreases with increasing buoy separation, even with constant ice cover properties. The apparent attenuation for short waves is also sensitive to the strength of the wind field. It decreases with increasing wind with a shift of the rollover to larger periods. This study indicates the importance of wind input and nonlinear interaction in interpreting measured apparent wave attenuation, particularly for short waves.

Results shown in this study are based on the specific choice of the source term parameterization available in WW3. For S_{ice} , both the viscoelastic model used in this study and the scattering model used in Perrie and Hu [1996] yield the same qualitative phenomenon. The impact of various S_{in} , S_{ds} and S_{nl} parameterizations on the results shown remains to be carefully examined.

Acknowledgements

The data used in this study are all provided in the references cited. This study was made possible by financial support from the National Key R&D Program of China (Nos.2016YFC1401405 and 2016YFC1402001) and from National Natural Science Foundation of China (No. U1406401). The Southern Ocean data were obtained with funding from National Institute of Water and Atmosphere Research Ltd. New Zealand, through core funding under the National Climate Centre Climate Systems programme. Weddell Sea data were obtained as part of the UK Natural Environment Research Council project "Short Timescale Motion of Pancake Ice" (STiMPI) Grant No. GR3/12952 aboard the F/S Polarstern during the ANT-17/3 cruise leg. Further analysis was funded under the Office of Naval Research "Sea State" Departmental Research Initiative, Grant No. N00014-13-1-0290 and N00014-13-1-0294, the Ministry of Education, Singapore through the AcRF Tier 2 Grant MOE2013-T2-1-054. In-kind support from the Office of Naval Research Global Grant N62909-15-1-2069 is also appreciated.

References

- Bennetts, L. G. and V. A. Squire (2012), Model sensitivity analysis of scattering-induced attenuation of ice-coupled wave, *Ocean Model.*, 45-46, 1-13, doi:10.1016/j.ocemod.2012.01.002.
- Cheng, S., X. Zhao, W. E. Rogers, J. Thomson, H. H. Shen (2016), Preliminary Calibration of a Rheological Sea Ice Model for Wave-In-Ice using Field Data, *Proc. 23rd IAHR International Symposium on Ice*, Ann Arbor, Michigan USA.
- Doble, M. J., M. D. Coon and P. Wadhams (2003), Pancake ice formation in the Weddell Sea, *J. Geophys. Res.*, 108, (C7)3209, doi: 10.1029/2002JC001373.
- Doble, M. J. and P. Wadhams (2006), Dynamical contrasts between pancake and pack ice, investigated with a drifting buoy array, *J. Geophys. Res.*, 111, C11S24, doi: 10.1029/2005JC003320.

Doble, M. J. and J.-R. Bidlot (2013), Wave buoy measurements at the Antarctic sea ice edge compared with an enhanced ECMWF WAM: Progress towards global waves-in-ice modelling, *Ocean Model.*, 70, 166-173, doi:10.1016/j.ocemod.2013.05.012.

Doble, M. J., G. de Carolis., M. H. Meylan, J-R Bidlot and P. Wadhams (2015), Relating wave attenuation to pancake ice thickness, using field measurements and model results, *Geophys. Res. Lett.*, 42(11), 4473-4481, doi:10.1002/2015GL063628.

Hasselmann, S. and K. Hasselmann (1985), Computations and parameterizations of the nonlinear energy transfer in a gravity-wave spectrum, Part I: A new method for efficient computations of the exact nonlinear transfer integral, *J. Phys. Oceanogr.*, 15, 1369–1377.

Kaleschke, L., and S. Kern (2006), Sea-ice concentration for Arctic & Antarctic (ASI-SSMI), *Integrated Data Climate Center*. [Available at http://icdc.zmaw.de/seaiceconcentration_asi_ssmi.html.]

Kohout, A. L. and M. H. Meylan (2008), An elastic plate model for wave attenuation and ice floe breaking in the marginal ice zone, *J. Geophys. Res.*, 113, C09016, doi:10.1029/2007JC004434.

Kohout, A. L., and M. J. M. Williams (2013), Waves-in-Ice Observations Made During the SIPEX II Voyage of the Aurora Australis, 2012, Australian Antarctic Data Centre, Australia. [Available at <http://dx.doi.org/10.4225/15/53266BEC9607F>.]

Kohout, A. L., M. J. M. Williams, S. M. Dean, and M. H. Meylan (2014), Storm-induced sea-ice breakup and the implications for ice extent, *Nature*, 509(7502), 604–607, doi:10.1038/nature13262.

Kohout, A. L., B. Penrose, S. Penrose, and M. J. M. Williams (2015), A device for measuring wave induced motion of ice floes in the Antarctic marginal ice zone, *Ann. Glaciol.*, 69(59), doi:10.3189/2015AoG69A600.

Li, J., A. L. Kohout and H. H. Shen (2015), Comparison of wave propagation through ice covers in calm and storm conditions, *Geophys. Res. Lett.*, 42(14), 5935-5941, doi: 10.1002/2015GL064715.

Liu, A. K. and E. Mollo-Christensen (1988), Wave propagation in a solid ice pack, *J. Phys. Oceanogr.*, 18(11), 1702–1712, doi: 10.1175/1520-0485(1988)018<1702:WPIASI>2.0.CO;2.

Liu, A. K., C. Y. Peng and P. W. Vachon (1991), Wave Attenuation in the Marginal Ice Zone During Limex. Geoscience and Remote Sensing Symposium, 1991. IGARSS '91. Remote Sensing: Global Monitoring for Earth Management., International (Vol.3, pp.1601-1604). IEEE.

Masson, D. and P. H. Leblond (1989), Spectral evolution of wind-generated surface gravity waves in a dispersed ice field, *J. Fluid Mech.*, 202, 43–81, doi:10.1017/S0022112089001096.

Meylan, M. H., L. G. Bennetts, and A. L. Kohout (2014), In situ measurements and analysis of ocean waves in the Antarctic marginal ice zone, *Geophys. Res. Lett.*, 41, 5046–5051, doi:10.1002/2014GL060809.

Newyear, K. and S. Martin (1999), Comparison of laboratory data with a viscous two-layer model of wave propagation in grease ice, *J. Geophys. Res.*, 104(C4), 7837-7840.

Perrie, W. and Y. Hu (1996), Air-Ice-Ocean Momentum Exchange, Part I: Energy Transfer between Waves and Ice Floes, *J. Phys. Oceanogr.*, 26, 1705-1720, doi: 10.1175/1520-0485(1996)026<1705:AMEPTB>2.0.CO;2.

Rogers, W. E. and S. Zieger (2014), New wave-ice interaction physics in WAVEWATCH III®. Proc. 22nd IAHR International Symposium on Ice, Singapore.

Rogers, W. E., J. Thomson, H. H. Shen, M. J. Doble, P. Wadhams and S. Cheng (2016), Dissipation of wind waves by pancake and frazil ice in the autumn Beaufort Sea, *J. Geophys. Res. Oceans*, 121, doi:10.1002/2016JC012251.

Saha, Suranjana, et. al. (2010), The NCEP Climate Forecast System Reanalysis. Bull. Amer. Meteor. Soc., 91(8), 1015-1057, doi: 10.1175/2010BAMS3001.1.

Saha, Suranjana and Coauthors (2014), The NCEP Climate Forecast System Version 2. J. Climate, 27, 2185-2208, doi: 10.1175/JCLI-D-12-00823.1.

Squire, V. A. (2007), Of ocean waves and sea-ice revisited, *Cold Reg. Sci. Technol.*, 49, 110–133.

Tolman, H. L. and D. V. Chalikov (1996), Source terms in a third-generation wind-wave model, *J. Phys. Oceanogr.*, 26, 2497–2518.

Tolman, H. L. (2003), Treatment of unresolved islands and ice in wind wave models, *Ocean Model.*, 5(3), 219–231, doi:10.1016/S1463-5003(02)00040-9.

Tolman, H. L. and the WAVEWATCH III® Development Group (2016), User manual and system documentation of WAVEWATCH III® version 5.16, NOAA Technical Note, MMAB Contribution No. 329, 361p.

Wadhams, P. (1975), Airborne laser profiling of swell in an open ice field, *J. Geophys. Res.*, 80(33), 4520-4528.

Wadhams, P. (1978), Wave decay in the marginal ice zone measured from a submarine, *Deep-Sea Res.*, 25(1), 23-40.

Wadhams, P. (1986), The seasonal ice zone, In *The Geophysics of Sea Ice* (ed. N.Untersteiner), Proc. NATO Advanced Study Inc. on Air-Sea Interaction in the Presence of Ice, Maratea, 26 Sept - 10 Oct 1981. Plenum Press, New York. 825-991.

Wadhams, P., V. A. Squire, J. A. Ewing and R. W. Pascal. (1986), The effect of the marginal ice zone on the directional wave spectrum of the ocean, *J. Phys. Oceanogr.*, 6(2), 358-376.

Wadhams, P., V. A. Squire, D. J. Goodman, A. M. Cowan and S. C. Moore (1988), The attenuation rates of ocean waves in the marginal ice zone, *J. Geophys. Res.*, 93(C6), 6799–6818, doi:10.1029/JC093iC06p06799.

Wang, R. and H. H. Shen (2010), Experimental study on surface wave propagating through a grease-pancake ice mixture, *Cold Reg. Sci. & Tech.*, 61(2-3), 90-96, doi:10.1016/j.coldregions.2010.01.011.

Wang, R. and H. H. Shen (2010), Gravity waves propagating into an ice-covered ocean: A viscoelastic model, *J. Geophys. Res.*, 115(C6), 302-315, doi:10.1029/2009JC005591.

Zhao, X., S. Cheng and H. H. Shen (2015), Modeling ocean wave propagation under sea ice covers, *Acta Mechanica Sinica*, 31(1), 1–15.

Accepted Article

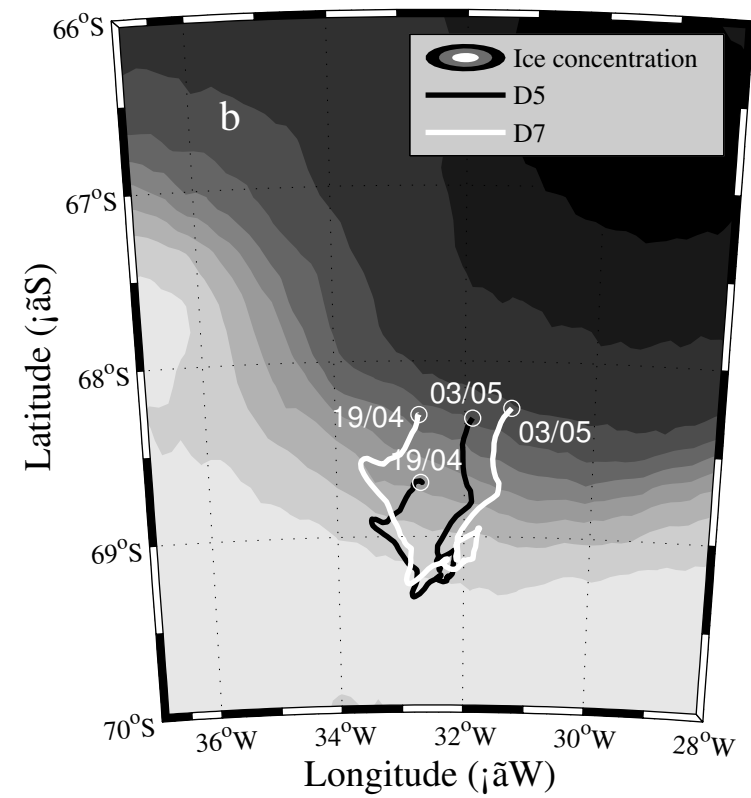
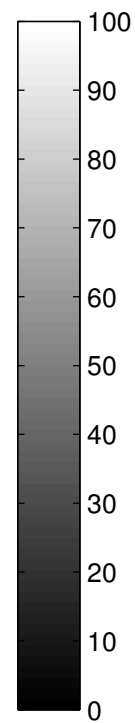
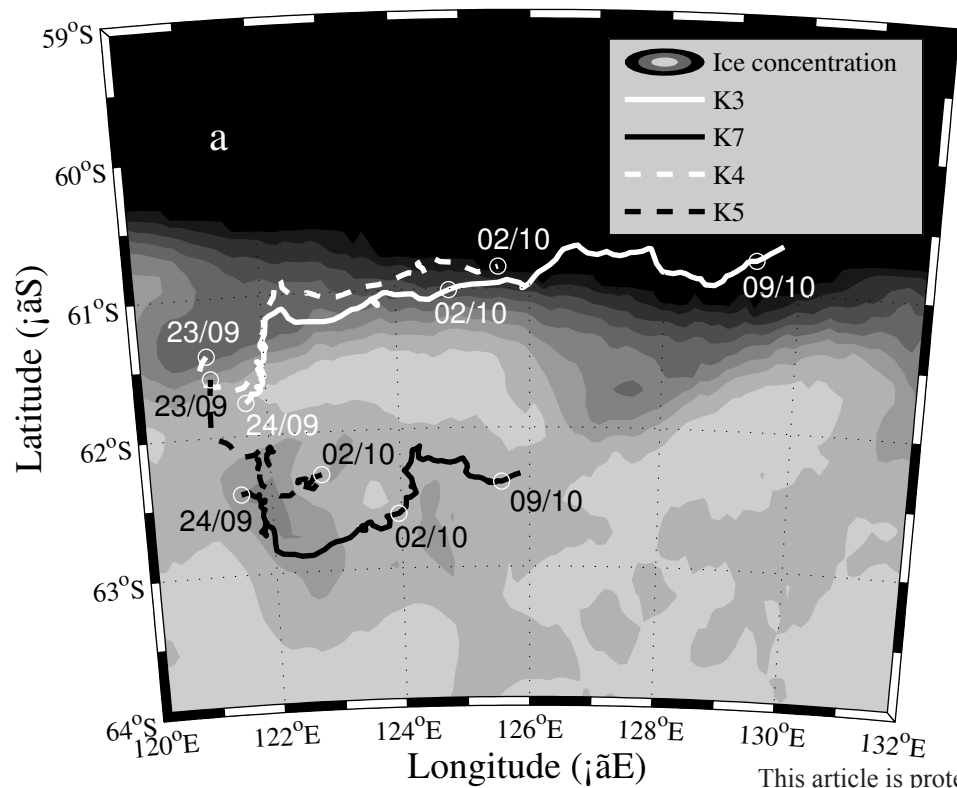


Figure 2.

Accepted Article

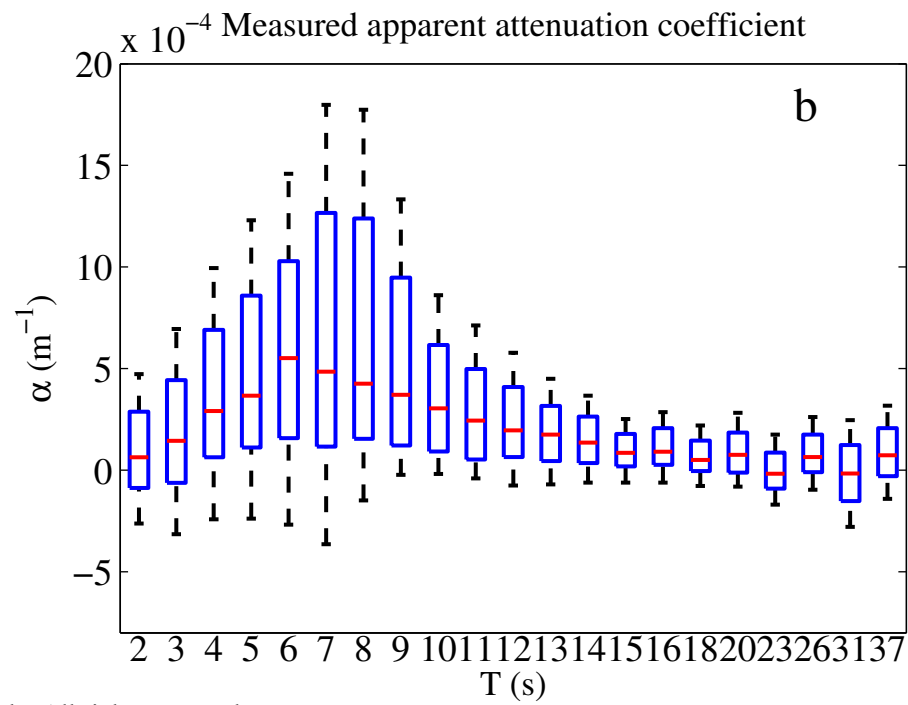
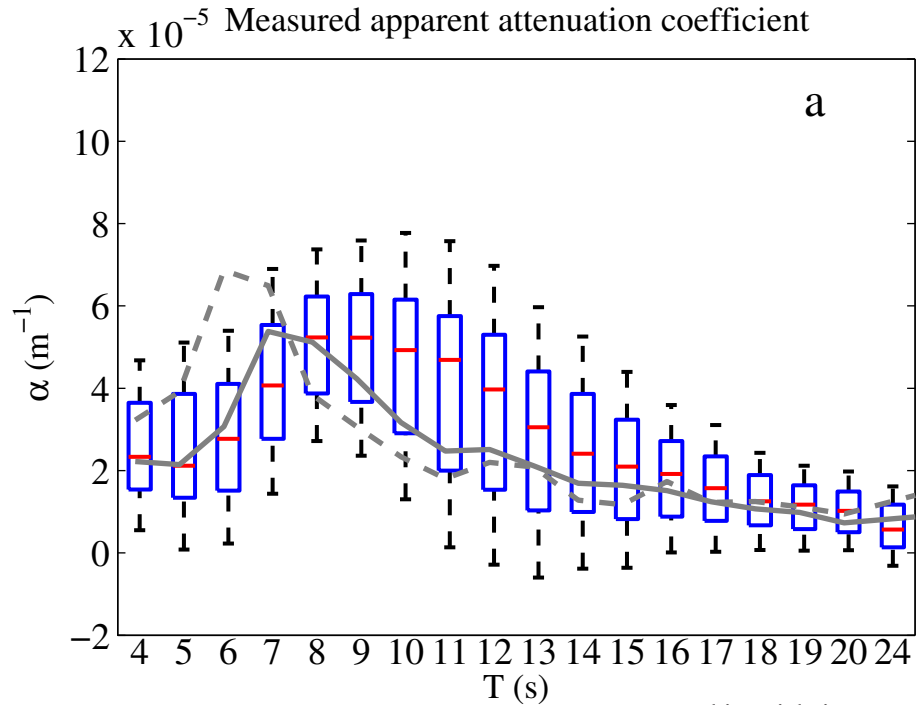
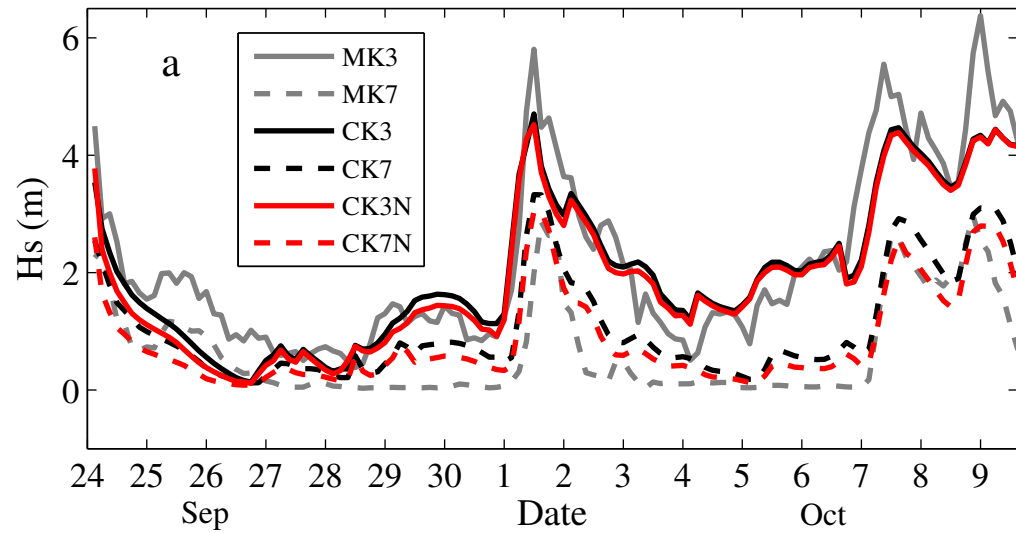


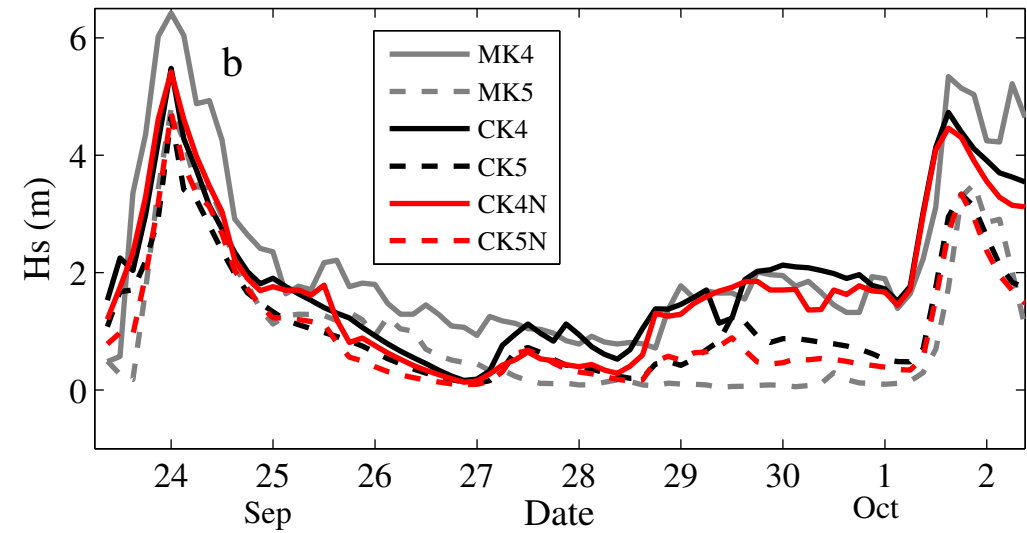
Figure 3.

Accepted Article

Sensor K3 & Sensor K7



Sensor K4 & Sensor K5



Sensor D7 & Sensor D5

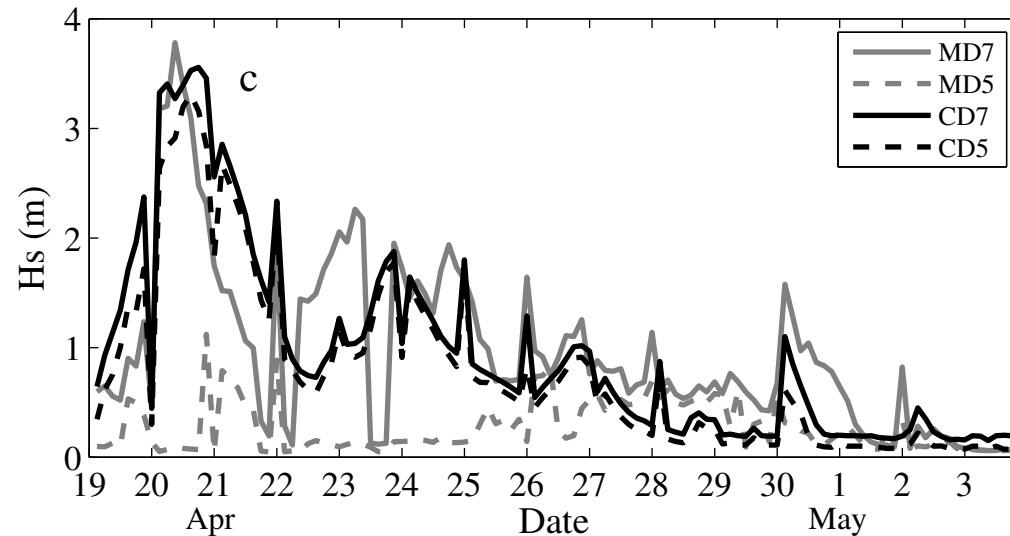


Figure 4.

Accepted Article

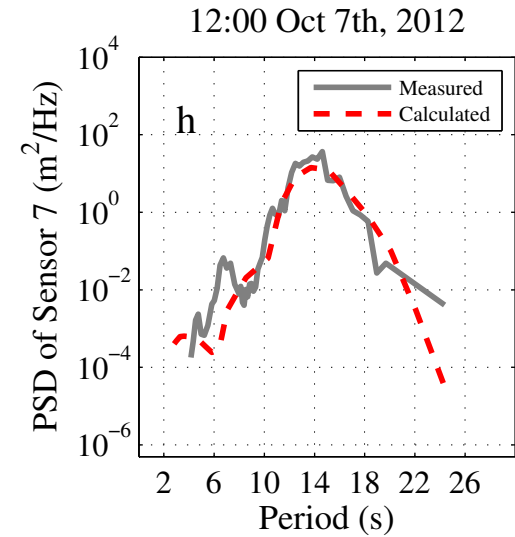
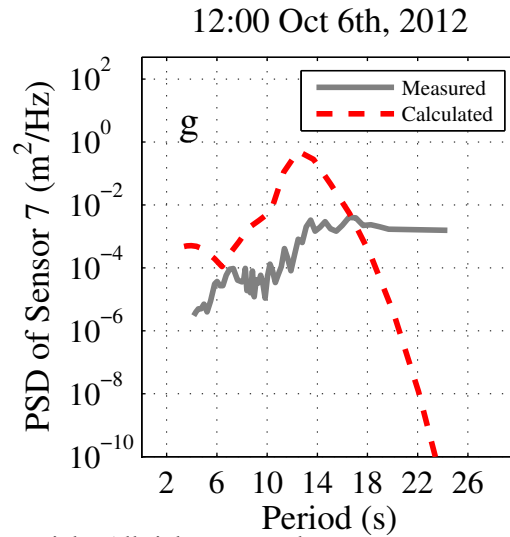
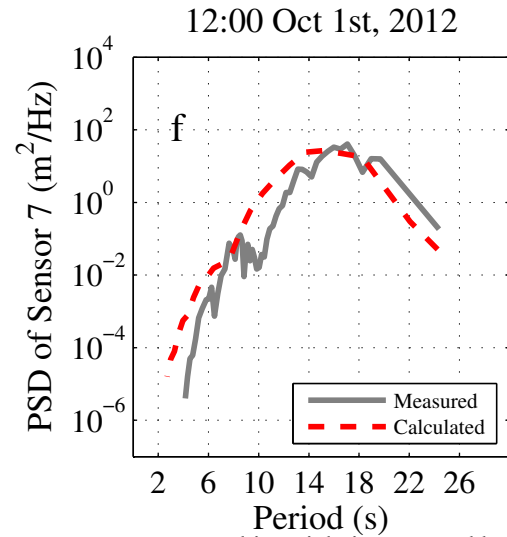
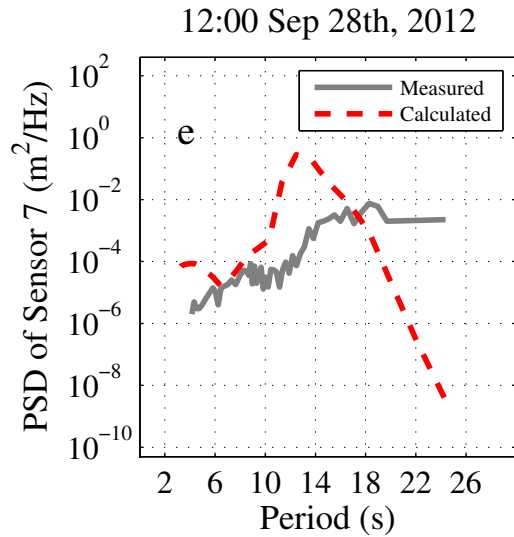
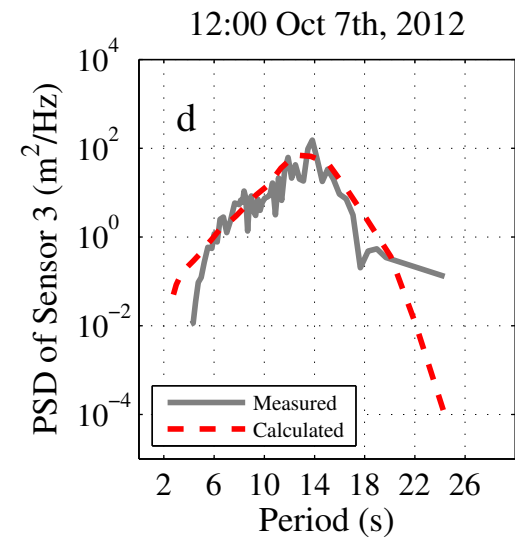
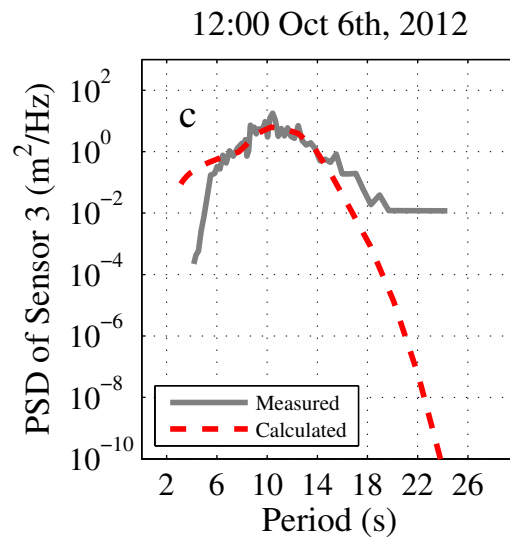
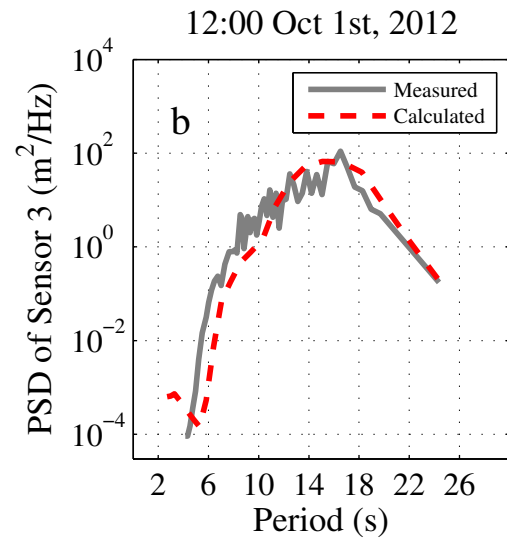
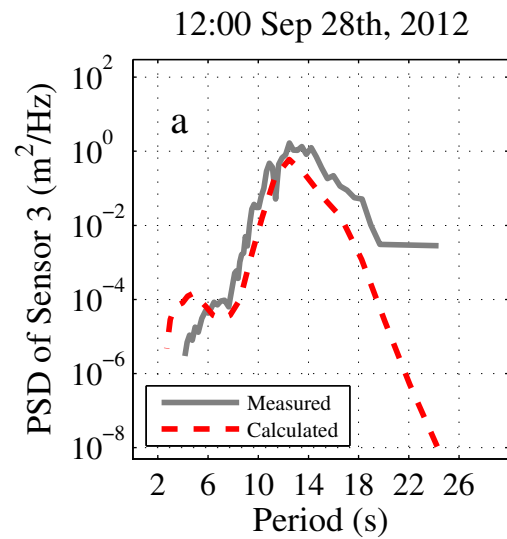


Figure 5.

Accepted Article

Apparent attenuation coefficient with IC3

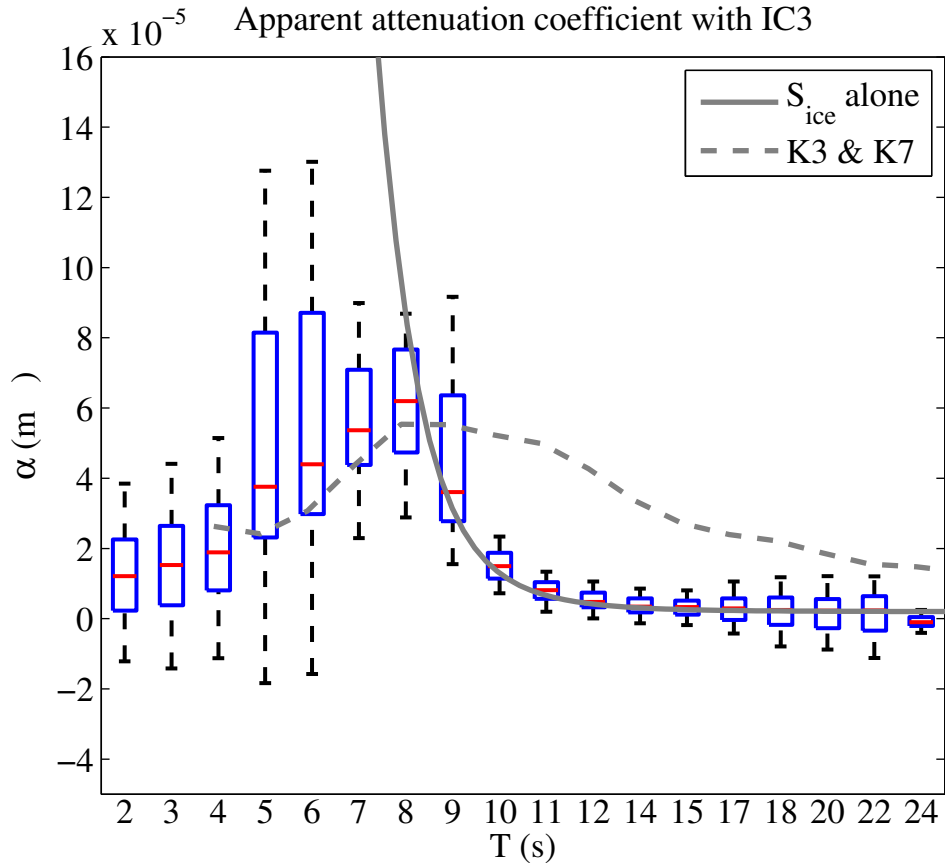


Figure 6.

Accepted Article

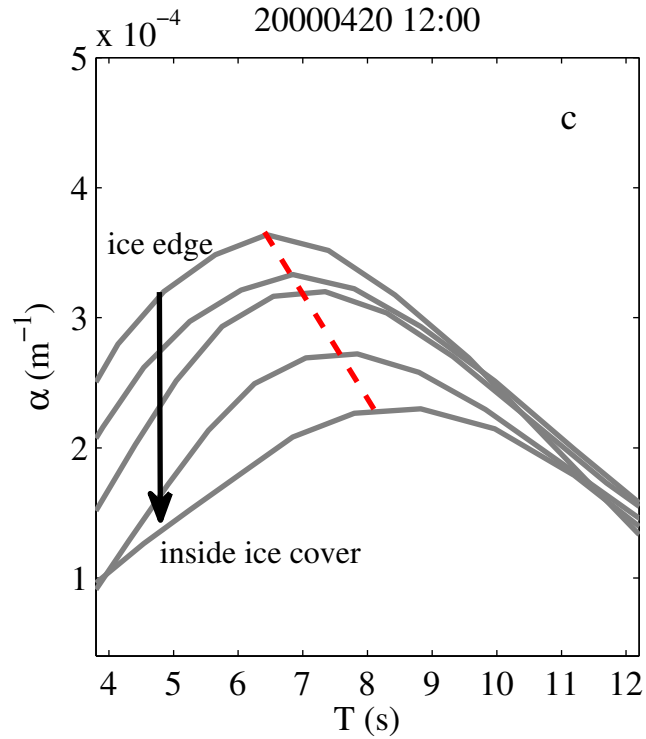
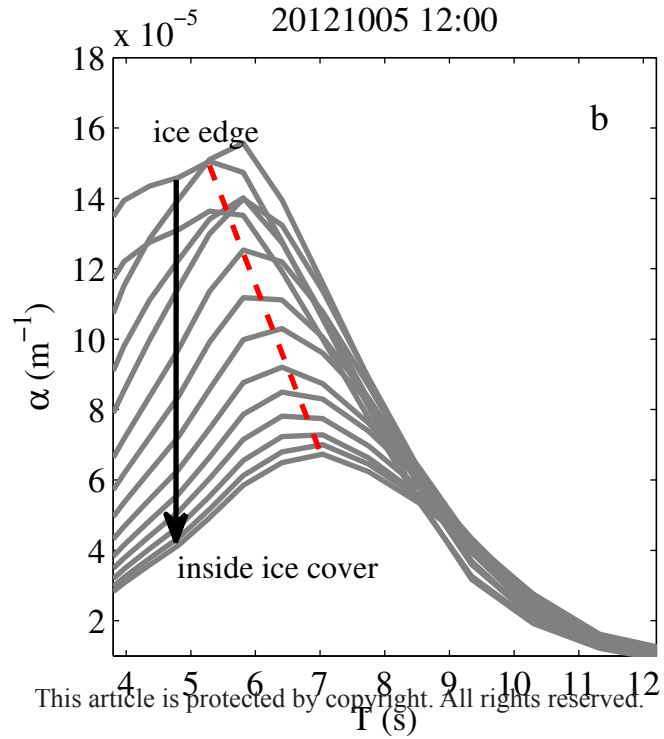
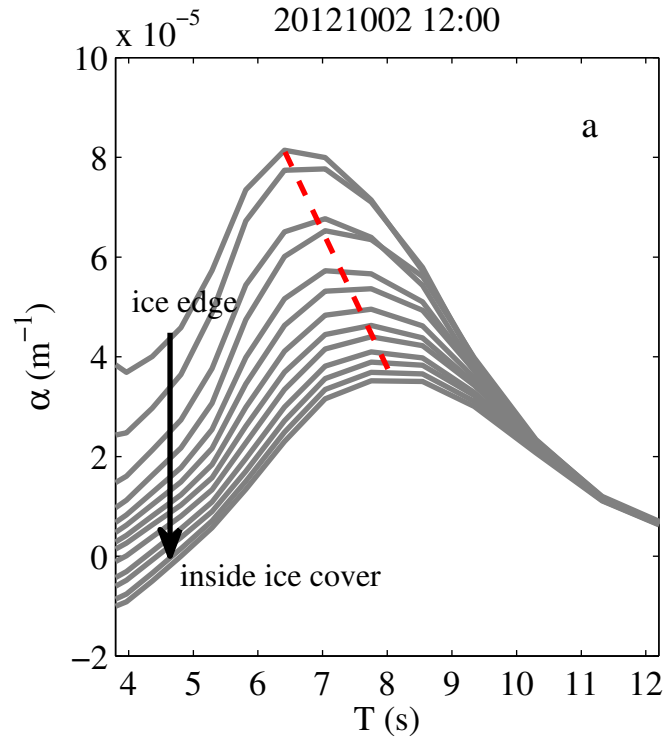


Figure 7.

Accepted Article

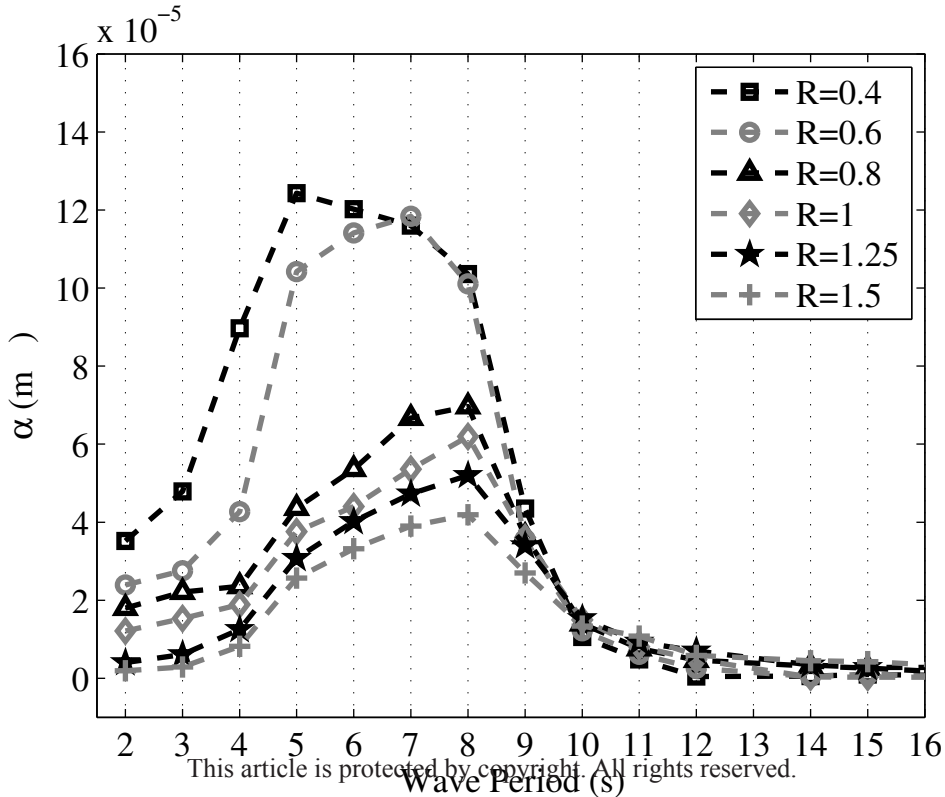


Table 1. Forcing data information

	wind	Ice thickness	Ice concentration
Case A	CFSv2 (Saha et al., 2014)	CFSv2 (Saha et al., 2014)	ASI-SSMI (Kaleschke and Kern, 2006)
	3-hr, $0.2^\circ \times 0.2^\circ$	3-hr, $0.2^\circ \times 0.2^\circ$	24-hr, 12.5 km^2
Case B	ECMWF ERA-Interim wind	CFSR (Saha et al., 2010)	ASI-SSMI (Kaleschke and Kern, 2006)
	6-hr, $0.125^\circ \times 0.125^\circ$	6-hr, $0.3^\circ \times 0.3^\circ$	24-hr, 12.5 km^2